Applied Thermal Engineering 236 (2024) 121699

Contents lists available at ScienceDirect

Applied Thermal Engineering

journal homepage: www.elsevier.com/locate/ate

Research Paper

Development of an air cooling system with low material budget for high-energy physics applications

Aitor Amatriain [a,b,*], Massimo Angeletti [a], Corrado Gargiulo [a], Gonzalo Rubio [b,c]

[a] ALICE Collaboration, CERN, Geneva 23, 1211, Switzerland
[b] E.T.S. Ingeniería Aeronáutica y del Espacio, Universidad Politécnica de Madrid, Plaza Cardenal Cisneros 3, 28040, Madrid, Spain
[c] Center for Computational Simulation, Universidad Politécnica de Madrid, Campus de Montegancedo, Boadilla del Monte, 28660, Madrid, Spain

ARTICLE INFO

Keywords:
Large Hadron Collider
ALICE experiment
Material budget
Air cooling
Carbon foams

ABSTRACT

This work presents the cooling system of a future particle detector at the Large Hadron Collider (LHC): the Inner Tracking System 3 (ITS3) of the ALICE experiment. Efficient cooling is crucial for maximizing the particle measurement quality in the LHC. The system introduces open-cell carbon foams as heat exchangers that combine heat conduction and convection for the first time in a high-level engineering application. The system is designed to have an unprecedentedly low material budget, which is a requirement for particle detectors aiming at precise tracking at low particle momenta. This novel approach leads to a 80% reduction of the material budget compared to the previous version (ITS2), resulting in enhanced measurement accuracy. The study employs an experimental wind tunnel setup and numerical simulation, showing excellent agreement with mean deviations under 0.5 K that are attributed to sensor installation uncertainties. The results confirm the system adherence to the temperature requirements. Compared to the baseline design, it is shown that enhancements based on numerical simulations produce potential reductions of up to 50% in the maximum temperature variation of the detector layers.

1. Introduction

The designs of cooling systems involve facing Conjugate Heat Transfer (CHT) engineering problems; that is, the heat transfer between liquids and solids with thermal coupling. These systems are frequently based on convection with single phase flows, namely in oil systems of turbofan engines [1] and in turbine blades [2]. Two-phase flows are employed for hybrid vehicle electronics [3]. Conductive heat transfer is the main mechanism in superconducting magnet energy storage systems [4]. The use of heat exchangers with both single- and two-phase flows is extensive [5], as the design possibilities are wide, and different materials can be used depending on the design requirements. In particular, materials such as open-cell foams are used, which are cellular structures that consist of a solid material that contains a ligament structure with a high number of pores [6]. Due to their high mechanical and thermal properties per unit of mass, these materials are an excellent choice for cooling applications [7,8].

In the High-Luminosity phase of the Large Hadron Collider (HL-LHC) at CERN – which will start in 2030 – new particle detectors will operate in three large experiments (ATLAS [9,10], CMS [11], and ALICE [12]). The cooling systems of these detectors will use open-cell carbon foams. In the baseline design – present in ATLAS and CMS – the heat dissipated by the sensors will be transferred by conduction to an open-cell foam and a titanium pipe, to then be removed by convection with two-phase CO_2. Additional structures of carbon fiber-reinforced plastic (CFRP) of reduced thickness will be added to increase structural stiffness (see Fig. 1).

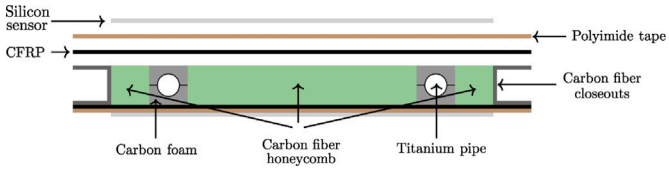

Fig. 1. Internal structure of the stave core of the ATLAS ITk Strip Detector [10].

The reason for using open-cell carbon foams in high-energy physics (HEP) is related to the radiation length, X_0, which is characteristic of each material [13]. For a given material thickness, the uncertainty of the measurement of the momentum of charged particles increases as the radiation length of the material is decreased. This is measured by the *material budget*, which is the ratio between the thickness of a detector layer, X, and the radiation length of its material (X/X_0). The overall

* Corresponding author at: ALICE Collaboration, CERN, Geneva 23, 1211, Switzerland.
E-mail address: aitor.amatriain@cern.ch (A. Amatriain).

https://doi.org/10.1016/j.applthermaleng.2023.121699
Received 13 June 2023; Received in revised form 30 August 2023; Accepted 25 September 2023
Available online 29 September 2023

performance of a tracking detector improves when the material budget is reduced [13]. The mean value in the baseline design of Fig. 1 is $X/X_0 \approx 0.6\%$ [10]. A variant of the system presented in Fig. 1 with thinner sensors, used in the current Inner Tracker (ITS2) of the ALICE experiment, has a material budget of $X/X_0 \approx 0.28\%$ [14]. Improvements of the baseline design are being developed such as the use of microchannels [15] and microvascular networks [16], although the reduction of the material budget is limited due to the use of support structures.

Obtaining material budget values lower than 0.25% requires the use of alternative cooling solutions. When power dissipation is lower than approximately 10^3 W m^{-2}, forced gas flow cooling emerges as alternative. The requirement of installing pipes around the detector is removed, providing the minimum material budget among all the cooling systems mentioned. Gas flow cooling was used in the Heavy Flavor Tracker (HFT) of the STAR experiment at the Relativistic Heavy Ion Collider (RHIC), where the detector power dissipation was equal to 1700 W m^{-2}. With a flow with a freestream velocity $v_\infty = 10$ m s^{-1}, the maximum temperature variation in the detector was 15 K [17]. However, the material budget in the inner layer was still high and non-uniform (≈0.4%), as a result of the contributions of cables and mechanical supports. In the Mu3e experiment, helium at $v_\infty = 10$–20 m s^{-1} will be used to remove the heat flux of 2500 W m^{-2} dissipated by the silicon tracker [18,19]. The use of aluminized kapton foils as structural supports will provide a lower material budget than the systems described previously ($X/X_0 \approx 0.11\%$).

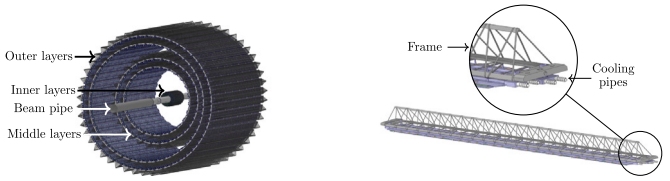

(a) Isometric view. (b) Structure of the OB staves.

Fig. 2. ALICE Inner Tracking System 2.

This work is focused on on the cooling system of the Inner Tracking System (ITS) of the ALICE experiment. The ITS is the closest detector to the beam pipe, where particle collisions are produced. Currently, the ITS2 is conceived as a two-barrel structure: the Inner Barrel (IB), formed by Layers 0 to 2, and the Outer Barrel (OB), formed by Layers 3-4 (middle layers) and Layers 5-6 (outer layers) (see Fig. 2(a)). The layers are azimuthally segmented into units named staves, which are mechanically independent. Each stave contains a Flexible Printed Circuit (FPC) that includes sensors and passive components: the Hybrid Integrated Circuit (HIC), the cooling pipes, and a frame (see Fig. 2(b)).

During the Long Shutdown 3 (2026–2030), a new IB with the three innermost layers (Layer 0 to Layer 2) will replace the current IB of the ITS2 [12]. The ITS3 IB will consist of two halves, named half-barrels, to allow the detector to be mounted around the beam pipe (see Fig. 3(a)). Each half-barrel will incorporate three layers made of a single large silicon pixel chip of length 280 mm and thickness of 40 µm, which will be bent into half-cylindrical shape. Moreover, a beryllium beam pipe of

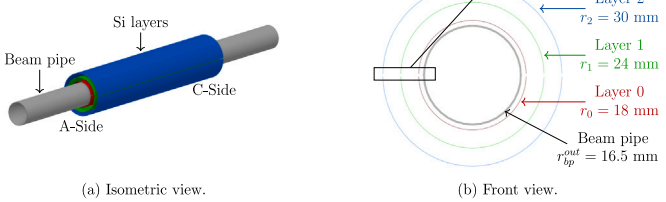

(a) Isometric view. (b) Front view.

Fig. 3. Inner barrel of the ALICE ITS3.

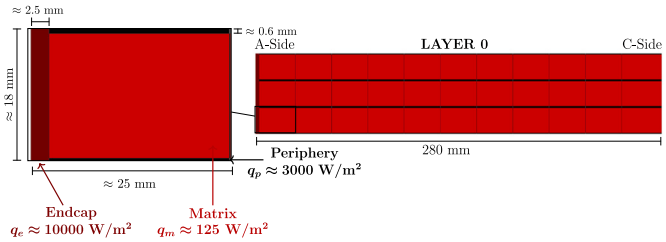

Fig. 4. Power dissipation in the silicon layers of the ALICE ITS3.

inner radius 16 mm and wall thickness of 500 µm will replace the one of the ITS2 of 870 µm of the same material.

Due to dimensional tolerances and space limitations in the detector installation, the half-layers will probably not be in contact, and currently the nominal distance between them is assumed to be 1 mm (see Fig. 3(b)). At one of the edges (A-Side, see Fig. 3(a)), the silicon sensors will be electrically interconnected over a length of approximately 300 µm to a flexible printed circuit using aluminum wedge wire bonding. Additional electrical components will be needed in that zone – called *endcap* – whose extension in the longitudinal (x) direction will be approximately 2.5 mm. In the endcap, the heat flux of the silicon sensor due to the power dissipation of the electrical components will be the highest (see Fig. 4). The rest of the sensor will be composed mainly by the *matrix*, which is the effective zone for particle detection, and where the heat flux is one order of magnitude lower than in the endcap. Each of the three layers of Monolithic Active Pixel Sensors (MAPS) silicon sensors are produced by stitching smaller parts of dimensions of around 18 mm × 24 mm, called stitching units [20]. The power will be transferred to the endcap region in the longitudinal strips called *peripheries*. Layer 0 is shown in Fig. 4, and the same schematic applies to Layers 1 and 2. Heat dissipation in the beam pipe, q_{bp}, is also expected. The value depends on the different characteristics of particle collisions, and inputs received from other groups consider $q_{bp} \leq 1000$ W m^{-2}. The heat flux values mentioned in this paragraph are approximate, and, in particular, spatially-averaged values; for example, the power dissipation in the periphery is expected to depend on the longitudinal coordinate.

The main cooling requirement of the ALICE ITS3 is the minimization of the thermal expansion of the silicon layers, as the accuracy of the sensors is between 4 and 6.5 µm; that is, a thermal deformation of more than 4 µm is detrimental to the measurement quality. Furthermore, there is a mismatch between the thermal expansion coefficient of silicon (CTE $\approx 2.5 \times 10^{-6}$ K^{-1}) and the standard epoxy glues (CTE $\approx 50 \times 10^{-6}$ K^{-1}), which are needed for the foam-silicon interfaces. Thus, temperature gradients generate stresses that should not affect the performance of the system. A maximum layer temperature variation $\Delta T = T - T_\infty = 10$ K is the upper limit set, while values closer to 5 K are considered a target. The temperature variation is referred to the ALICE cavern (room) temperature T_∞, which is constant throughout the detector operation, and its absolute value does not affect the performance of the system. Consideration of relative temperatures is due to the fact that the detector is installed and calibrated at T_∞, and the cooling air is extracted from that region. Thus, the system is in zero-stress condition at $\Delta T = 0$, and the freestream air temperature is equal to the room temperature.

In this work, we present the novel cooling system used in ALICE ITS3, which will be the first particle detector at CERN to utilize a cooling system based on forced air convection. The high heat flux in the endcap will be dissipated with the use of open-cell foams. The cooling system must also ensure that the layers are kept into cylindrical shape, which implies the use of structural supports. Carbon foams are chosen for the supports to minimize the material budget, with a mean value per layer of $X/X_0 \approx 0.06\%$. This is the lowest value ever

achieved in a HEP particle detector, with a reduction of 80% with respect to the ITS2 ($X/X_0 \approx 0.28\%$). Multiple studies are available in the literature on the characterization of open-cell carbon foams, in particular for the foams to be used in the ALICE ITS3 [8]. Open-cell foams have been reported as potential candidates to be used in different fields such as electronic devices [21], heating, ventilation, and air conditioning (HVAC) systems [22], and solar power plants [23]. However, to the authors' knowledge, the use of open-cell foams as heat exchangers that combine heat conduction and convection is still not present in high-level engineering applications. This work presents a novel application in HEP, and covers in Section 2 the development steps that are applicable to other engineering areas. The process is based on following numerical and experimental approaches, and the corresponding results are compared and discussed in Section 3. This section includes parametric studies and a proposal for an improvement in design. Finally, the main conclusions of this work are listed in Section 4.

2. Methodology

The development of the ALICE ITS3 cooling system is divided into three parts: first, the design is explained in Section 2.1, which is focused on the thermal and structural parts to be used in the silicon half layers; then, the design proposed is built and installed in a wind tunnel setup that is discussed in Section 2.2; finally, a mathematical model is developed in Section 2.3 that is used to validate the thermal performance of the system.

2.1. ALICE ITS3 cooling system

The heat dissipated by the sensors will be removed by an air flow. To reduce the temperature gradients in the endcap region (see Fig. 4), the proposed design considers the use of thermally-conductive open-cell carbon foam rings in that zone, in contact with the silicon sensors. The foams act as heat exchangers, so that the heat is transferred from the sensors to the foams by conduction, and then it is removed from the foams by air convection. The carbon foam rings in the endcap region are not sufficient to keep the silicon sensors into cylindrical shape, and the design includes additional foam parts that act as mechanical supports. These aspects of the design are detailed in Section 2.1.1. Since there are four air flow channels in the detector, the second decision is related to the air flow distribution system in Section 2.1.2.

2.1.1. Design

The cooling system uses two different types of open-cell carbon foams:

- Reticulated Vitreous Carbon (RVC) Duocel®: one of morphological structures of the vitreous carbon manufactured by ERG Aerospace. This foam is a thermal insulator (see Table 1), although its low density and high specific Young modulus E motivate its use as a structural part [8]. The cell structure is isotropic, consisting of multiple cells with the geometry of a tetrakaidecahedron: a 14-sided truncated octahedron [8] (see Fig. 5(a)).
- K9: this foam manufactured by Lockheed Martin is made of RVC as a base material, with graphite added by chemical vapor deposition to increase its thermal conductivity κ_f (see Table 1). The porosity Φ is still low despite the addition of the graphite. The microscopic structure is the same as the one of the RVC, with smaller mean cell size ℓ_{cell} (see Fig. 5(b)), which gives a high specific surface area Σ_f. This is beneficial for the conductive heat transfer, since the heat transfer rate is proportional to this parameter [8].

In the baseline design, RVC and K9 foams are used as follows (see Fig. 6(a)):

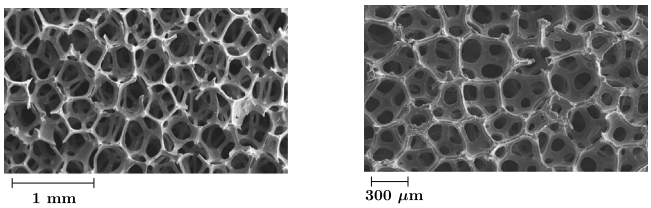

(a) RVC. (b) K9.

Fig. 5. Microscopy images of the carbon foams used in the ALICE ITS3 cooling system [8].

Table 1
Parameters of the foams to be used in the ALICE ITS3 cooling system.

Foam	ρ (kg/m^3)	Φ	l_{cell} (m)	Σ_f (1/m)	κ_f (W/(m K))	E (Pa)
RVC	45	0.97	3.9×10^{-4}	6600	0.05	10^8
K9	200	0.89	2.85×10^{-4}	14700	25	4×10^8

- A-Side: three rings made of the K9 foam are placed. The length of the rings in the x direction is 6 mm, which is the same as the distance between the layers. This is the minimum value determined from mechanical tests at CERN so that there are no risks of breaking the foams in the assembly process. It is not possible to place a fourth ring in the 1.5 mm height channel between the beampipe and Layer 0 due to design tolerances.
- Plane $y = 0$: no thermal performance is required in that zone, therefore longerons made of the RVC foam are used near the edges of the silicon sensors. The dimension in the y direction of these foams is 2.5 mm.
- C-side: since there is no endcap region, rings of the same geometry of those of the A-Side made of RVC foam are placed.

To leave space for the wire bonding procedure, as a conservative approach, the A-side rings are not placed in contact with the endcap region, and a spacing ζ of 2.5 mm is left (see Fig. 6(b)); that is, there is no contact between the 2.5 mm long endcap and K9 foam. In regard to the foam-silicon interface, following previous experimental studies [8], carbon fleece of 120 μm of thickness and areal density of 8 g m^{-2} is placed between the silicon layers and the foams. Considering the material budget, the shear strength, and the thermal performance, a compromise solution has been taken with a glue layer of 100 μm between the fleece and the heater, and a glue penetration of 250 μm in the foam. The Araldite 2011 epoxy glue is used in the RVC foam, and the Epoxies® 50-3150 FR (epoxy adhesive filled with Al_2O_3 powder) in the K9 foam.

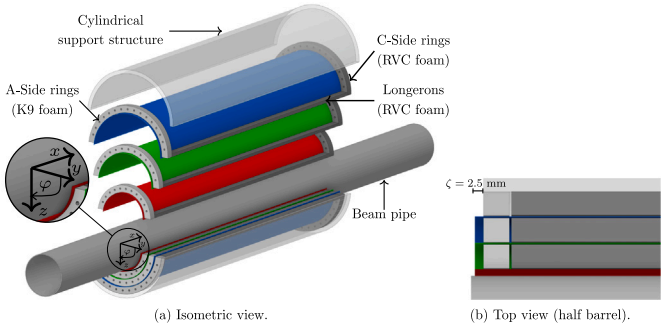

(a) Isometric view. (b) Top view (half barrel).

Fig. 6. Foam structures of the inner barrel of the ALICE ITS3.

Due to the complexity of the installation of the ITS3 in the ALICE cavern, the system is not expected to be completely isolated, therefore pressure drop of the foams should be minimized to reduce leaks. This also reduces the power required by the flow distribution system. To this end, holes are drilled into the foams as shown in Fig. 6(a). The diameter of the holes is 1.5 mm.

2.1.2. Air flow distribution

In terms of ease of installation and integration with other subsystems, the simplest approach is to use a single channel at the inlet (see Fig. 7).

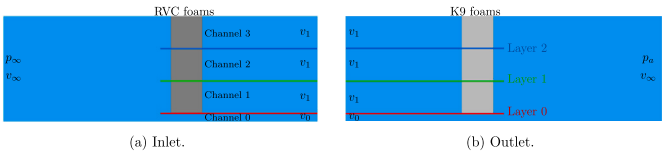

(a) Inlet. (b) Outlet.

Fig. 7. Single flow distribution. Cut with the plane $x = 0$.

Since carbon foam rings produce pressure losses, the flow distribution in the four channels is a priori unknown. An estimation can be obtained by making the following assumptions:

- The flow is steady and one-dimensional.
- The pressure loss due to friction forces on the walls of channels 1, 2, and 3 is negligible compared to the pressure loss induced by the foams.
- The pressure loss of a foam with 1.5 mm holes is 20% lower than that of a foam without holes. These values are obtained from [8].
- The velocity in the three outermost channels is the same and equal to v_1. This is because the channel height and the foams used in each channel are the same, so the flow resistance is the same in all three channels.
- The flow in the beam pipe-L0 channel is turbulent with a Reynolds number $\rho v_0 h_0/\mu > 10^3$, with h_0 referring to the channel 0 height, and the pressure loss is given by the Darcy–Weisbach equation with a conservative friction factor $f = 0.1$ [24].
- The pressure at the outlet p_a is the same for the four channels.

The flow distribution is such that the pressure loss $p_\infty - p_a$ is minimized across the channels. The velocity in the channel 1 (v_0) and the one in the channels 1, 2, and 3 (v_1), which is reached at a sufficient distance downstream of the rings, is shown in Table 2. Since v_0 is one order of magnitude greater than v_1 in all cases, it is not possible to have an adequate control of the velocity distribution. It is concluded that it is necessary to have a minimum of two distribution channels: one for channel 0, and another for channels 1, 2, and 3.

Table 2
Flow distribution in the ALICE ITS3 with a single distribution channel.

v_∞ (m/s)	v_0 (m/s)	v_1 (m/s)
2	27.12	1.22
4	46.45	2.86
6	64.55	4.56
8	82.21	6.29
10	99.64	8.03

2.2. Experimental setup

An experimental setup has been built at CERN to study the thermal performance of the design explained in Section 2.1.1. Moreover, the assembly procedure – which is not described in this work – is a crucial part of the design, and this setup contributes to the process optimization. The silicon bending and the performance in-house gluing procedure explained in Section 2.1.1 require the use of parts with tight tolerances, as well as high-precision tools such as optical microscopes.

Fig. 8(a) shows the core of the setup, which consists of a prototype of a half-barrel of the design of Fig. 6(a) and a carbon sandwich cover (CFRP+thermally-insulating foam+CFRP). The cover has an inner radius of 40 mm, instead of the 36 mm required (30 mm of radius of Layer 2 shown in Fig. 3(b) + 6 mm of the foam). This is because it was previously manufactured for a preliminary model of 40 mm of inner radius, and it was decided to adapt it to the current design. To solve the mismatch in the dimensions, a thermally-insulating closed-cell carbon foam is introduced to cover the remaining 4 mm of thickness (see Fig. 8(c)). The final prototype will be manufactured as a single part of CFRP. All thermal interfaces with the aluminum supports have a thick layer of a thermally-insulating epoxy glue to reduce the thermal losses of the system. The choice of aluminum instead of 3D-printed parts for the support is related to the tolerances of the assembly process.

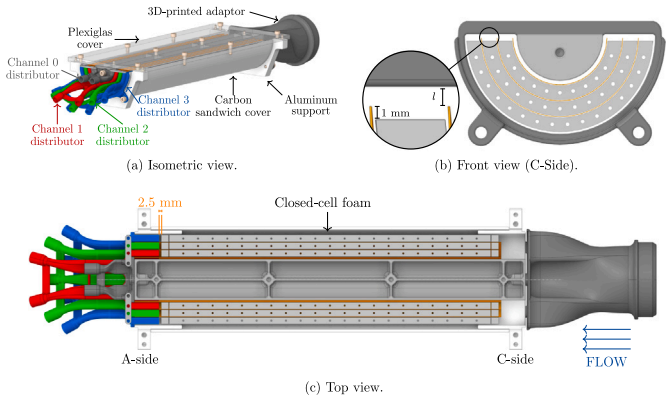

(a) Isometric view. (b) Front view (C-Side).

(c) Top view.

Fig. 8. ITS3 half barrel used in the experimental setup.

A flow distribution system consisting of four separate channels has been designed (see Fig. 8(a)). The longitudinal distance from the distribution channels to the foams is 2.5 mm (see Fig. 8(c)), which is the minimum to allow a conservative space of 2.5 mm of the endcap region is left for the wire bonding procedure. As shown in Fig. 8(b), the foam rings cover an azimuth angle – defined in Fig. 6(a) – of $\varphi_0 < \varphi < \varphi_1$ with $\varphi_0 > 0$ and $\varphi_1 < \pi$, since in the assembly process a gap of 1 mm is required at the edges (see Fig. 8(b)). The distribution system is such that it covers also $\varphi_0 < \phi < \varphi_1$, therefore it cannot be seen from the C-side (see Fig. 8(b)). This configuration has been chosen to minimize the air flow in the zone of height $l + 1$ mm and maximize the amount of air that flows through the foams at the A-side. The distance between the edge of the layers and the plexiglas cover is $l = 1.5$ mm in the experimental setup, although in the real detector the distance to the symmetry plane will be $l = 0.5$ mm (see Fig. 3(b)). The gap of ≈1 mm between the outermost ring and the cover shown in Fig. 8(b) is filled with glue. At the C-side, the transition from a circular pipe of 25 mm of radius to the prototype of 16.5 mm of inner radius and 36 mm of outer radius is done with a 3D-printed adaptor. The detailed geometry of the adaptor is not relevant for the current work. This is because even if the adaptor modifies the flow at the inlet, the low characteristic length of the RVC foam (see Table 1) acts as a flow straightener. Moreover, the flow that passes through the foam holes is independent of the inlet flow, due to the lower characteristic length and the high velocity gradients that are generated when the air flows through the holes. In addition, the pressure loss induced by the adaptor is negligible against the foam pressure loss.

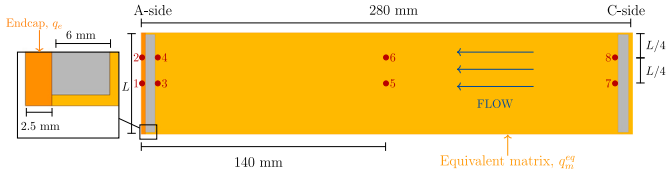

Fig. 9. Location of the temperature sensors in each layer.

The heat dissipated by the silicon sensors is modeled with integrated heaters that contain a silicon wafer of 40 μm, a copper heater of 5 μm, and three polyimide layers of 12.5 μm (polyimide-silicon-polyimide-copper-polyimide). The layers are joined with an epoxy glue. The measured total thickness of the heaters is between 160 and 170 μm, and the exact thickness of each of the glue layers is unknown. Since the thermal conductivity of epoxy glues is approximately the same

as the one of polyimide ($\kappa = 0.2\ \mathrm{W\,m^{-1}\,K^{-1}}$), the glue layers are considered as additional thickness of 27.5 μm of the polyimide layers. Thus, the equivalent system of the simulations consists of five layers, with a thickness of 40 μm of the polyimide layers, and a total thickness of 40 μm (silicon) + 3 × 40 μm (polyimide) + 5 μm (copper) = 165 μm. As shown in Fig. 9, the heater of each layer is divided into two resistors. The first one is the endcap with a heat flux equal to q_e. The periphery region is not considered, and its effect is included as an additional power dissipation in the second resistor called "equivalent matrix", with a heat flux equal to q_m^{eq}. The layout of the foam-integrated heater interface is the same as that explained in Section 2.1.1, but replacing the silicon by the integrated heaters. In all integrated heaters, the temperature of the polyimide layer in contact with the silicon layer is measured with eight PT1000 temperature sensors with an uncertainty of ±0.15 K. These sensors are joined to polyimide layers using the same glue used in the foam-heater interface (see Fig. 9). Sensors 1 to 4 are placed in contact with the foam. Holes of 1.5 mm of diameter are drilled in the longerons so that the wires of the temperature sensors can exit the system (see Fig. 8(c)).

A computed tomography (CT) scan has been performed at CERN to verify the cylindricity of the layers of the experimental setup. Fig. 10(a) shows a comparison between the scan (white) and the layers from the CAD model (red, green, and blue), and shows that the proposed design ensures the correct shape of the silicon sensors. The results have been post-processed with CAD software. The conclusion is that the difference between the CAD model and the experimental setup is negligible in all regions except small zones near the edges; in particular, at the edge of Layer 0, where the maximum deviation is 100 μm. The cause of this deviation is attributed to a non-optimal mechanical interface between the RVC foam and the silicon sensors, as shown in Fig. 10(a). This problem can be solved by increasing the contact surface between the foam and the silicon; that is, either increasing the size of the foam, or using a denser foam. The CT-scan also shows that the gluing process developed at CERN ensures to have an optimum uniform glue layers (see Fig. 10(b)).

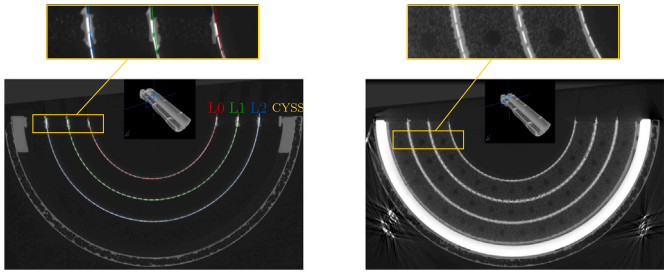

(a) CT scan and CAD comparison - Matrix. (b) CT Scan - A-side.

Fig. 10. Results of the Computed Tomography scan performed at CERN.

The air flow is generated by a fan that can provide up to 2×10^4 Pa for a freestream velocity of 20 $\mathrm{m\,s^{-1}}$, and includes a frequency inverter so that the operating point can be set manually or with a computer. All channels are equipped with an aluminum valve and a mass flow meter that have an uncertainty of $\pm 0.07 v_\infty$ (see Fig. 11(b)). Channel 3 uses two mass flow meters due to limitations in the range of the devices. The mean freestream velocity in the four half-barrels $v_{\infty,i}$ (i from 1 to 4) is obtained by mass conservation assuming that the flow is steady and incompressible. The valves have been designed and produced at CERN to minimize the pressure loss in that area. Due to space limitations in the installation of the ITS3 in the ALICE cavern, the fan must be placed close to the A-side. Thus, the fan operates such that the flow direction is from the C-side to the A-side (see Fig. 8(c)); that is, the air expands when flowing through the system. This decision is justified because, in the opposite operating condition – where the fan blows air – the inlet temperature is higher than the room temperature. This is a consequence of the non-isentropic expansion that is produced by the fan, which is not desirable.

The inlet of the system is a pipe of 50 mm of inner diameter that contains a grid to straighten the flow and reduce the turbulence levels (see Fig. 11(a)). The inlet and outlet temperatures are measured by temperature sensors of the same model as those of the heaters. A velocity sensor is installed to verify that there are no leaks in the system, and that the values given by the mass flow meters are correct. The difference between the mass flow given by the velocity sensor and the sum of the values obtained from the mass flow meters is 5%, which is of the order of the sensor accuracy. The straight pipes where the temperature sensors are installed are made of PVC, and the flexible pipe that joins the fan and the outlet straight pipe is made of silicon. The same material is used for the white pipes that connect the 3D-printed manifold and the valves, while the black pipes connected at both sides of the mass flow meters are 3D-printed.

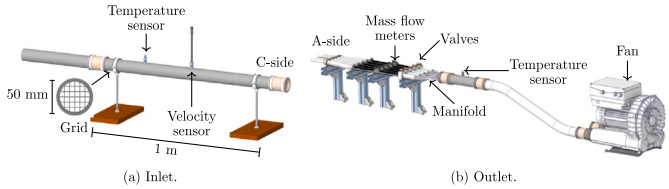

(a) Inlet. (b) Outlet.

Fig. 11. Components of the wind tunnel.

2.3. Mathematical model

The mathematical model consists of the governing equations introduced in Section 2.3.1 that are closed by the boundary conditions defined in Section 2.3.2. The numerical implementation is explained in Section 2.3.3.

2.3.1. Equations

The incompressible Reynolds-averaged Navier–Stokes (RANS) equations for the air are [25]:

$$\begin{cases} \nabla \cdot \langle \boldsymbol{v} \rangle = 0 & \text{(a)} \\ \rho \left(\frac{\partial \langle \boldsymbol{v} \rangle}{\partial t} + \langle \boldsymbol{v} \rangle \cdot \nabla \langle \boldsymbol{v} \rangle \right) = -\nabla \langle p \rangle + \nabla \cdot [(\mu + \mu_t) \nabla \langle \boldsymbol{v} \rangle] + \langle \boldsymbol{S} \rangle & \text{(b)} \\ \rho c_p \left(\frac{\partial \langle T \rangle}{\partial t} + \langle \boldsymbol{v} \rangle \cdot \nabla \langle T \rangle \right) = \nabla \cdot [(\kappa + \kappa_t) \nabla \langle T \rangle] + \langle Q \rangle, & \text{(c)} \end{cases} \tag{1}$$

where $\langle \boldsymbol{v} \rangle$ is the mean velocity, t is the time, $\langle p \rangle$ the mean pressure, μ the dynamic viscosity, c_p the specific heat at constant pressure, $\langle T \rangle$ the mean temperature, and κ the thermal conductivity. Eqs. (1)(a) to (1)(c) also contain the following assumptions, terms, and parameters:

- The flow regime depends on the air freestream velocity, which is a priori not fixed. The model assumes that the flow is turbulent in all cases simulated, and the turbulent viscosity μ_t derived from the Boussinesq assumption is provided by the $k-\omega$ SST turbulence model. The model combines the strong points of the $k-\omega$ model (highest near wall-accuracy), and the $k-\varepsilon$ model (highest outer region accuracy) [26]. It also includes a $\tilde{y}^+$-insensitive wall modeling explained in Section 2.3.2.
- The *mean viscous dissipation function* $\langle \phi_v \rangle = \nabla \cdot (\langle \tau \rangle \cdot \langle \boldsymbol{v} \rangle) - \langle \boldsymbol{v} \rangle \cdot (\nabla \cdot \langle \tau \rangle)$ that contains the mean viscous stress tensor $\langle \tau \rangle$ is neglected, since in terms of the Mach number $M^2/Re \ll 1$.
- The *mean source term* $\langle \boldsymbol{S} \rangle$ takes into account the pressure loss of foams [27]:

$$\langle \boldsymbol{S} \rangle = \Phi \left(\frac{\mu}{\mathcal{P}} + \frac{\Phi \rho C_d}{\sqrt{\mathcal{P}}} |\langle \boldsymbol{v} \rangle| \right) \langle \boldsymbol{v} \rangle \, \mathbf{1}_{\Omega_f}. \tag{2}$$

where Φ is the foam porosity and $\mathbf{1}_{\Omega_f}$ is the indicator function in the foam domains. The first component (Darcy's law) represents the drag of Stokes flows ($Re \ll 1$), while the second component (Forchheimer's law) provides the general expression for $Re \gg 1$,

with $\mathcal{P}$ and C_d referring to the permeability and the drag coefficients, respectively. The values $\mathcal{P}_{RVC} = 3.32 \times 10^{-9}$ m^2, $\mathcal{P}_{K9} = 5.97 \times 10^{-10}$ m^2, $C_{d_{RVC}} = 7.81 \times 10^{-2}$, and $C_{d_{K9}} = 1.02 \times 10^{-1}$ are obtained from [8].

- The *turbulent thermal conductivity* $\kappa_t = \mu_t c_p / Pr_t$, where $Pr_t = 0.85$ is the turbulent Prandtl number obtained from [28].
- The air and the solid material of the foams are considered to be an homogeneous mixture. Based on the theory of multiphase flows [29], the *specific enthalpy* of the foam is:

$$\underbrace{\rho_f h_f}_{\text{Foam}} = \underbrace{\Phi \rho c_p (T - T_{\text{ref}})}_{\text{Air}} + \underbrace{(1-\Phi)\rho_s c_s (T_s - T_{\text{ref}})}_{\text{Solid}}, \tag{3}$$

where $T_{\text{ref}} = 298.15$ K is the reference temperature, and T_s the solid temperature.

- In the foam domains, the air temperature is given by Eq. (1)(c), and the *mean heat source* $\langle Q \rangle$ models the convective heat transfer:

$$\langle Q \rangle = h \Sigma_f (T_s - \langle T \rangle) \mathbf{1}_{\Omega_f}. \tag{4}$$

Since the RVC foam is a thermal insulator (see Table 1), the heat flux from the silicon layers to the RVC foam is negligible, and in this foam the thermal equilibrium model is considered: $\langle T \rangle = T_s$. In the K9 foam, the heat transfer coefficient h is obtained from the Nusselt number $Nu = h l_{\text{cell}} / \kappa = C_h Re_{l_{\text{cell}}}^n$, where $C_h = 0.56$ and $n = 0.51$ [8]. The variable T_s refers to the solution of the energy equation in the solid material of the foam:

$$(1-\Phi)\rho_s c_s \frac{\partial T_s}{\partial t} = \kappa_f \nabla^2 T_s + h \Sigma_f (\langle T \rangle - T_s) \mathbf{1}_{\Omega_f}. \tag{5}$$

- All layers of the integrated are coupled with the foams and the fluid domain. The interfaces between the foams and the heaters are modeled as a single layer of glue of equivalent thickness of 250 μm derived from previous studies [8]. The heat equation is solved in all the layers mentioned, and the dissipated heat is implemented as a source term equal to the heat flux divided by the layer thickness.

2.3.2. Boundary conditions

Boundary conditions are defined at the inlet, outlet, walls, and the domain symmetry plane.

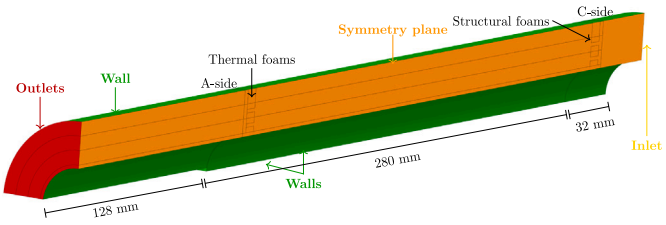

Fig. 12. Computational domain of the simulations.

Inlet

The inlet of the domain is placed at the outlet of the 3D-printed adaptor shown in Fig. 8(a). The numerical results are not sensitive to variations of the geometry, as expected from the arguments explained in Section 2.2. At the inlet, the pressure is set to the reference pressure, and a Neumann boundary condition is used for the velocity and the RANS turbulence variables. The static temperature is set to T_∞.

Outlets

The geometry is simplified in this region, and the length of the channels is extended 128 mm away from the A-side foam. This length value is such that the flow is uniform at the outlets. Simulations have been performed with the real geometry of the distribution channels (see Fig. 8(a)), and the $\Delta T = T - T_\infty$ values in the eight locations of the temperature sensors (see Fig. 9) have been compared. The results have shown that the differences between the results given by the two geometries are lower than 1%. This difference is assumed to be lower than the error related to other assumptions of the model, such as those related to the modeling of the interfaces between different materials. With the simplified geometry of Fig. 12, the mass flow rate is defined at the four outlets, where the velocity is equal to the freestream velocity v_∞. Zero-gradient boundary conditions are used for the pressure, the temperature, the turbulent kinetic energy, and the turbulent dissipation rate.

Walls

No-slip condition and adiabatic boundary conditions are imposed, and the turbulent kinetic energy is set to zero. The dimensionless wall-parallel mean velocity is given by the solution at the viscous sublayer: $\langle v^+ \rangle_\parallel = \tilde{y}^+$, where $\tilde{y}^+$ is the dimensionless wall distance. The boundary condition for ω is obtained from a perturbation analysis of the ω-equation [30]: $\omega^+ = 85/((\tilde{y}^+)^2)$.

Symmetry

The plane $y = 0$ (see Fig. 6(a)) is considered as symmetry plane.

2.3.3. Numerical implementation

Formulation and mesh

The system of equations is solved with the finite volume method that is implemented in Ansys Fluent 2023R1 [31]. The poly-hexcore method is used for meshing, which creates a mesh consisting of octrees in the bulk region, keeps a high-quality layered poly-prism mesh in the boundary layers, and connects these two meshes with general polyhedral elements.

The computational mesh is generated with different cell sizes. The coarsest size is set in the fully-developed region of the flow between the silicon layers, while the finest size is defined in the A-side. This is due to the strong interaction between the wake of the flow downstream of the carbon foams and that downstream of the channels of height $l + 1 = 2.5$ mm illustrated in Fig. 8(b). In the remaining flow regions, namely the fully-developed region of the channels of $l + 1 = 2.5$ mm in height, intermediate cell sizes are used. At all walls 10 cells are defined along the thickness of the boundary layers, with the wall $\tilde{y}^+ < 5$ to ensure the consistency of the wall treatment explained in Section 2.3.2.

All solid layers with high aspect ratio, such as those of the heaters, are implemented using the Shell Conduction model. This model does not require that the wall thickness is taken into account in the mesh generator. The solid layers mentioned are generated automatically by the Ansys Fluent solver before the simulation starts. The shells are adiabatic on the sides where there is no physical contact with other components, whereas the equality of the temperatures and heat fluxes is imposed elsewhere. In the shell-foam contacts, the shells are coupled with the solid domain of the porous medium.

Resolution of the equations

Flow variables are stored at cell centers, and the cell face values are obtained from interpolation schemes. A central differencing scheme is used for all terms of the equations except from the convective terms of the momentum and energy equations, for which a second-order upwind scheme is used. In the continuity equation, a corrected momentum interpolation is used to avoid pressure checkerboarding [32]. Gradients are obtained by a least-squares procedure, and a linearized form of each equation for the flow variable Φ is:

$$\rho V_{\text{cell}} \frac{\Phi^{n+1}_{\text{cell}} - \Phi^n_{\text{cell}}}{dt} + A^n_{\text{cell}} \Phi^{n+1}_{\text{cell}} = \sum_{nb} A^n_{nb} \Phi^{n+1}_{nb} + B^n_{\text{cell}}. \tag{6}$$

In Eq. (6), nb is used to denote neighbor cells, superindexes n and $n+1$ refer to the current and next time step, respectively, A and B are constants, and V_{cell} is the cell volume. Assuming that a steady solution is

reached, the unsteady term, discretized with an Euler implicit method with time step dt, constitutes a form of implicit under-relaxation. A coupled solver is used, in which continuity and momentum equations are solved simultaneously, while the remaining equations are solved separately [33]. The systems of linear algebraic equations are solved using an algebraic multigrid method that uses the Gauss–Seidel method as smoother [34]. The residuals of Eq. (6) in the mth iteration, which are globally-scaled, are defined as follows:

$$R_{\Phi}^{m} = \frac{\sum_{\text{cell}} |\sum_{nb} A_{nb} \Phi_{nb}^{m}|}{\sum_{\text{cell}} |A_{\text{cell}} \Phi_{\text{cell}}^{m}|}. \tag{7}$$

Temperature values are monitored in the eight sensor locations (see Fig. 9), and simulations are terminated when these values do not vary. It is verified that, at this point, the globally-scaled residuals are $<5 \times 10^{-4}$ (continuity), $<10^{-5}$ (momentum and turbulent variables), and $<10^{-8}$ (energy). These values are lower than those given by default in Ansys Fluent of $<10^{-3}$ (continuity, momentum, and turbulent variables) and $<10^{-6}$ (energy).

3. Results and discussion

First the accuracy of the model developed in Section 2.3 is assessed in Section 3.1. The data obtained from the experiment described in Section 2.2 is used for result comparison. The validated model is then used to simulate the real configuration and perform a parametric study focusing on the power dissipations of the layers in Section 3.2.

Table 3
Simulation parameters.

Symbol	Material	Parameter	Value	Units
c_p	Air	Specific heat at constant pressure	1006	J kg^{-1} K^{-1}
c_s	Be	Specific heat	1825	
	Cu		385	
	Glue		1000	
	K9		710	J kg^{-1} K^{-1}
	PI		1100	
	RVC		710	
	Si		710	
q_{bp}	Be	Heat flux in the beampipe	0	W m^{-2}
q_m^{eq}	Si	Heat flux in the equivalent matrix	250	W m^{-2}
q_e	Si	Heat flux in the endcap	10000	W m^{-2}
κ	Air	Thermal conductivity	0.025	W m^{-1} K^{-1}
	Be		216	
	Cu		385	
	Glue		0.85	
	K9 (κ_f)		25	
	PI		0.2	
	RVC (κ_f)		0.05	
	Si		149	
μ	Air	Dynamic viscosity	1.79×10^{-5}	Pa s
ρ	Air	Density	1.225	kg m^{-3}
	Be		1850	
	Cu		8930	
	Glue		1800	
	K9 (ρ_f)		200	
	PI		1420	
	RVC (ρ_f)		45	
	Si		2329	

The simulation parameters are shown in Table 3. The physical properties are obtained from [35] (Be), [36] (Si), [8] (foams), and by private communication with the suppliers of the polyimide (PI) and the glue. The thermal conductivity value of the glue tested at CERN is considered instead of the one provided by the official datasheet ($\kappa = 2.16$ W m^{-1} K^{-1}). The material properties are taken at $T_\infty = 293$ K, and their temperature dependence is neglected, since the temperature range studied is limited (293–303 K). The importance of considering relative temperatures has been stressed in the introduction; therefore, all results presented hereafter are temperature variations with respect to the freestream temperature, $\Delta T = T - T_\infty$.

Table 4
Mesh independence study of the numerical simulation.

$\delta_{\min}$	$\delta_{\max}$	Number of cells	ΔT_1 (K)	ΔT_3 (K)	ΔT_5 (K)	ΔT_7 (K)
$d/12$	$d/2$	1.1 M	7.11	2.62	3.93	1.46
$d/24$	$d/4$	4.6 M	7.37	2.69	3.77	1.38
$d/48$	$d/8$	18.3 M	7.43	2.71	3.74	1.33

As mentioned in Section 2.2, the integrated heaters contain no periphery regions, and their effect is considered applying a heat flux equal to the area-weighted average of the heat flux in the periphery ($q_p = 3000$ W m^{-2}) and in the matrix ($q_m = 125$ W m^{-2}). The surface areas of each region are calculated taking as reference the dimensions of the stitching unit (see Fig. 4).

3.1. Mathematical model validation

3.1.1. Mesh independence study

Three meshes of different element sizes are considered, with minimum and maximum element lengths equal to $\delta_{\min}$ and $\delta_{\max}$, respectively. These values refer to the distance between the layers $d = 6$ mm. In each mesh, the total number of cells considered in the study contains the cells generated by the Shell Conduction model. The freestream velocity $v_\infty = 5$ m s^{-1}, and the monitored temperature values are referred to Layer 1 in the locations shown in Fig. 9.

Table 4 shows that the temperature values vary only marginally when the mesh size is increased, halving $\delta_{\min}$ and $\delta_{\max}$, and even smaller differences are obtained by halving them further, demonstrating the tendence to converge. This is a reasonable result, since the flow around the layers is not complex, and in all cases the boundary layers contain 10 elements in the wall normal direction. This ensures a consistent behavior of the velocity and the turbulent variables in the context of RANS turbulence modeling. The medium mesh of 4.6 M cells is chosen due to the significant differences between the coarse and fine meshes in ΔT_1.

3.1.2. Comparison with experimental data

Figs. 13(a), 13(c) and 13(e) depict the temperature in the endcap region measured in the experiments and the one predicted by the numerical model proposed in this work. The mean difference (in L_1 norm) between the simulation curves and the temperature sensor value with lowest thermal resistance (highest temperature) is lower than 0.5 K. The simulations overpredict the temperature values in most cases, which is attributed to the thermal resistance produced by the glue between the polyimide layer and the temperature sensors. The glue thickness is estimated to be around 100–200 μm. While the experimental values of ΔT_3 and ΔT_4 differ less than 0.25 K, there are noticeable differences between ΔT_1 and ΔT_2, especially in Layers 0 and 2. Apart from the differences derived from the contact between the sensor and the layer, it should be noted that in the endcap region the temperature is not uniform. Thus, a small difference in the location of the sensor can produce differences as those shown here. Moreover, the planar dimensions of the sensors (1.6 × 1.2 mm) are of the same order as the endcap length (2.5 mm), leading to additional uncertainty in the measurements.

Figs. 13(b), 13(d) and 13(f) show the results given by the experiments and the simulations in the matrix region. Similar conclusions to those of the endcap region can be drawn when comparing experimental and numerical results. The temperature discrepancy between the sensors placed at constant values of the x coordinate are negligible except from ΔT_5 and ΔT_6 in Layer 2. In that case, it is assumed that the low ΔT_5 values are due to a bad contact between it and the polyimide layer. It should be noted that some of the experimental ΔT values are negative, which can be ascribed in part to the limited accuracy of the temperature sensors. Even if their accuracy is stated to be ±0.15 K by the official datasheet, when the heat dissipation is set to zero, a difference of 0.6 K

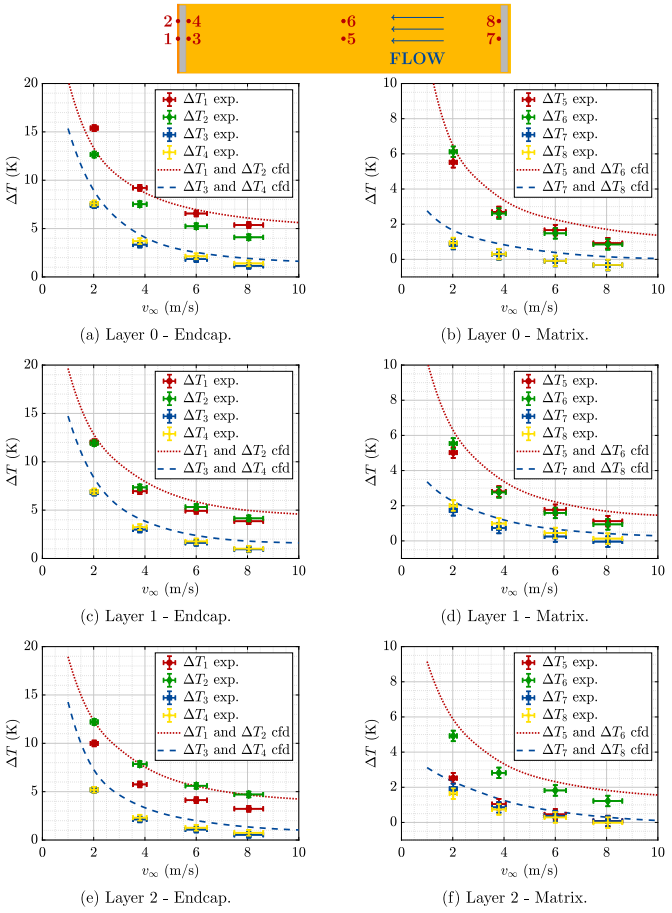

Fig. 13. Temperature variation with respect to the freestream temperature, in the polyimide layers that are in contact with the silicon layers. The heat fluxes are $q_m^{eq} = 250$ W m^{-2} and $q_e = 10\,000$ W m^{-2}.

has been obtained between the minimum and maximum values among all the 26 temperature sensors. Thus, the uncertainty of the temperature values of Fig. 13 is ±0.3 K. In addition, differences have been observed between the time scales of the inlet temperature and the temperature of the sensors, since the temperature of the test room is not constant during the tests.

Another important aspect to be taken into account is that, for channels 1, 2, and 3 (see Fig. 7), the Reynolds number of the fully-developed channel flow $Re = \rho v_\infty d/\mu = 2000$ for $v_\infty = 5$ m s^{-1}. Assuming that the division of flow regimes in circular pipes is applicable [37], the fully-developed channel flow is laminar for $v < 5$ m s^{-1}, and transitional for $5 < v_\infty < 10$ m s^{-1}. To justify the use of RANS, simulations have been performed to study the accuracy of the RANS model in the heat transfer of a periodic channel flow. The laminar case considers $\mu_t = 0$ with the use of a central differencing scheme for the convective terms of the momentum and energy equations to minimize the numerical diffusion. Laminar and RANS solutions have been compared, leading to the conclusion that the error introduced by the RANS model is negligible. This is reasonable, since $\mu_t/\mu \ll 1$ in the cases simulated with the turbulence model. The reason for using a RANS turbulence model in all cases is that the velocity increases in the region around the foam holes, and the resulting shear flow is turbulent for approximately $v_\infty > 1$ m/s in the mesh considered. In these cases, even if a Large Eddy Simulation approach is followed [25], the simulations do not reach a steady state due to the reduction in the turbulent viscosity. Performing unsteady simulations implies a large increase in the computational cost, which is discarded because of the reasonable accuracy of RANS in laminar heat transfer, as well as the fact that no time-dependent quantities are analyzed in the current study.

3.2. Real configuration of the ITS3 cooling system

The increase in temperature in the endcap region is the main concern, since the ΔT values are more than twice as those in the matrix region. However, the layout described in Section 2.2 is not the same as the one of the model that will be installed in the ALICE cavern, since the heaters include polyimide and glue layers that act as a thermal barrier. As previously mentioned, the distance to the symmetry plane will be $l = 0.5$ mm instead of $l = 1.5$ mm (see Fig. 8(b)). In addition, the detector will consist of two half-layers instead of one, with three zones of different power dissipation in the layers: the endcap, the periphery, and the matrix, unlike in the experimental setup, where only the endcap and the "equivalent matrix" are considered.

In this section the real configuration of the ITS3 will be simulated with the modifications mentioned in the previous paragraph. Apart from the $y = 0$ plane, in the current simulations the plane $x = 0$ is also a symmetry plane (see Fig. 6(a)): that is, 1/4 of the geometry is simulated. The air distribution system is the same as the one of the experimental model. The dimensions and values of the heat fluxes in the three regions are given in Fig. 4; in particular, the heat fluxes are $q_e = 10\,000$ W m^{-2}, $q_p = 3000$ W m^{-2}, and $q_m = 125$ W m^{-2}, which give the same total power dissipation as in the simulations of Section 3.1.2. In this configuration, the main objective is to verify in Section 3.2.1 that $\Delta T < 10$ K in all layers. Then, a parametric study is performed in Section 3.2.2 focused on the heat dissipations of the layers, and, finally, the weak point of the design will be identified and improved in Section 3.2.3.

3.2.1. Thermal analysis

The ΔT distribution in the silicon layers of the real configuration is shown in Fig. 14. In comparison to the results of Fig. 13, the ΔT in the endcap and matrix of the real configuration are 1-2 K higher. One of the reasons for the differences is that the polyimide layers of the integrated heaters produce a thermal resistance, which is not negligible since the polyimide is a thermal insulator. Furthermore, the layer temperature increases locally in the periphery regions. This is due to the locally increased power dissipation with respect to the matrix, which is a phenomenon that cannot be predicted in the experimental model.

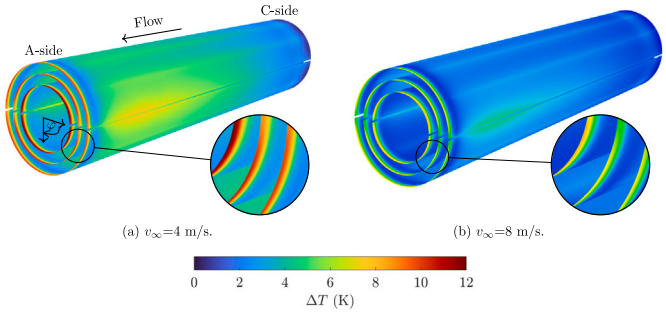

Fig. 14. Contours of the temperature variation with respect to the freestream temperature in the real configuration of the ITS3 layers.

The highest temperature values in the matrix and periphery regions are obtained close to $\varphi = 0$ at the C-side, since the trajectory of the air that flows through the channel of height 1.5 mm is deviated near the A-side. This is because, as previously pointed out, the flow distribution system does not cover the full π radians of the azimuth angle φ. In addition, there is no contact between the foam and the periphery region at $\varphi \approx 0$. It is deduced that values of $v_\infty > 4$ m s^{-1} are required to achieve $\Delta T < 5$ K in the matrix and periphery regions. An analogous conclusion can be drawn in the endcap, and, in particular, for approximately $v_\infty > 5$ m s^{-1}, the maximum temperature variation is lower than 10 K in all layers. Therefore, the design requirement stated in Section 1 is met.

3.2.2. Parametric study

No higher heat dissipation values than those used in the simulations are expected. However, as mentioned in Section 1, the values of the heat fluxes used in the simulations are approximate values averaged over the surfaces. Since the maximum ΔT in the endcap is close to the design limit of 10 K, it is essential to study the influence of the power dissipation in the endcap. In addition, the effect of the power dissipation of the beam pipe – which is not considered in the experimental setup – on the temperature distribution needs to be assessed, since it is of the same order as the matrix power dissipation.

Endcap

Taking as reference the baseline value of the endcap heat flux $q_0 = 10\,000\ \mathrm{W\,m^{-2}}$, the influence of this value on the mean endcap temperature variation is shown in Fig. 15. The dependence as a function of the heat flux and the freestream velocity follows the same behavior predicted by an analytical solution obtained in previous works: $\overline{\Delta T} = \overline{T}_e - T_\infty \sim q/\sqrt{v_\infty}$ [8]. As shown in Fig. 14, Layer 0 is the layer with the maximum temperature variation in all cases, and for $q \leq 3q_0/2$ it is not possible to achieve temperature differences smaller than 10 K.

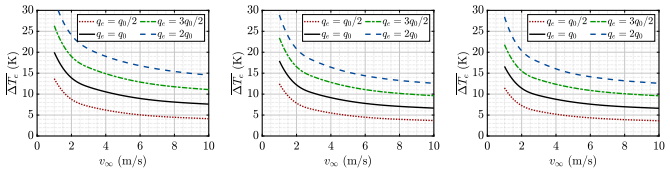

(a) Layer 0. (b) Layer 1. (c) Layer 2.

Fig. 15. Influence of the endcap power dissipation on the endcap mean temperature variations with respect to the freestream temperature.

The effect of the K9 foam at the A-side can be noticed in Fig. 14, as in the foam-layer zone the temperature variation is negligible. However, in the baseline configuration, where the endcap length is 2.5 mm and the foam is placed at a distance $\zeta = 2.5$ mm from the edge of the layer (see Fig. 6(b)), there is no physical contact between the foam and the endcap. This limits the performance of the system, given that the layer thickness is only 40 μm and conductive heat transfer is not effective despite the high thermal conductivity of silicon.

Beam pipe

Another key aspect mentioned in Section 1 is that the beam pipe is expected to dissipate heat due to particle collisions. Cooling the beam pipe is not a design requirement, although the beam pipe power dissipation leads to a temperature increase in the silicon layers; in particular, in Layer 0, which is the most critical based on the previous analyses. The effect of the beam pipe power dissipation is addressed by considering three cases in the range mentioned in Section 1. In all simulations of this study the power dissipations in the silicon layers are the same as the one in the baseline case.

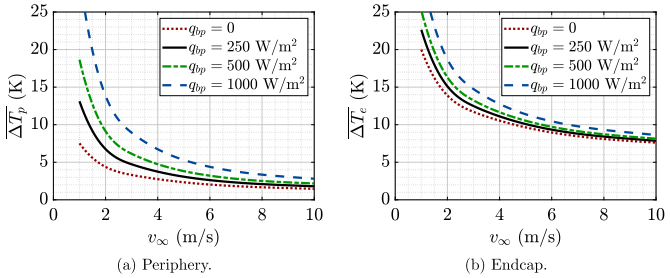

(a) Periphery. (b) Endcap.

Fig. 16. Influence of the beam pipe power dissipation on the Layer 0 mean temperature variations with respect to the freestream temperature.

Fig. 16(a) shows the influence of the beam pipe power dissipation, which increases when the freestream velocity is decreased. This is justified because the thickness of the thermal boundary layers is inversely proportional to this parameter, and the reduced distance between the beam pipe and Layer 0 contributes to the heat transfer, which is not negligible even for intermediate velocity values. The effect is less pronounced in the endcap (see Fig. 16(b)), since the power dissipation in that zone is one order of magnitude higher than in the beam pipe. However, since the temperature variation in Layer 0 is close to the design limit of 10 K, the effect of the beam pipe cannot be neglected. This strengthens the importance of the design improvement that will be discussed hereafter.

Table 5
Influence of the K9 foam position on the mean endcap temperature variation with respect to the freestream temperature for $v_\infty = 8\ \mathrm{m\,s^{-1}}$.

ζ (mm)	$\overline{\Delta T_e}$ (K)
2.5	8.12
1.5	5.39
0.5	4.06

3.2.3. Design improvement

As mentioned in Section 1, the baseline design is highly conservative. The wire bonding region extends 300 μm in the x direction. When the ITS3 is built, the wire bonding procedure will be carried out before the gluing of the carbon foams. Therefore, there will be no limitations in terms of spacing needed for the wire bonding. Thus, it is reasonable to move the carbon foams closer to the layer edge, to allow a physical contact between the endcap and the foam. The theoretical maximum length of the contact region is 2.2 mm: that is, 2.5 mm of the endcap minus 300 μm of the wire bonding. However, achieving this value is a challenge, since the wire bonding region is delicate, and a non-optimal gluing between the foam and the silicon can produce damages to the electronics. Consequently, apart from the baseline design where the endcap-foam contact length is zero ($\zeta = 2.5$ mm), two additional configurations will be studied. A limit case is considered by setting $\zeta = 0.5$ mm, which means a contact length of 2 mm between the foam and the silicon. The intermediate case is defined by $\zeta = 1.5$ mm, which means a contact length of 1 mm between the foam and the silicon.

Table 5 shows that the endcap temperature depends strongly on the K9 foam position in the A-side. This means that there is a high margin of improvement in the temperature variation in the endcap region. If a value of $\zeta \approx 1$ mm can be set, with the baseline power dissipation of $q_e = 10\,000\ \mathrm{W\,m^{-2}}$, $q_p = 3000\ \mathrm{W\,m^{-2}}$, and $q_m = 125\ \mathrm{W\,m^{-2}}$, and a freestream velocity $v_\infty = 8\ \mathrm{m\,s^{-1}}$, then the ΔT would be approximately uniform along the layers. Moreover, it would be bounded by 5 K, which implies almost a 50% reduction over the baseline configuration shown in Fig. 14(b).

4. Conclusions

In this work, the design of the cooling system for ALICE ITS3 has been presented. The system will use forced air cooling for the first time in an experiment at the Large Hadron Collider. The non-uniform heat dissipation within the layers has motivated the incorporation of carbon foams, which act as localized heat exchangers, combining conduction and convection. To the best of the authors' knowledge, this represents the first practical application in high-level engineering. These foams also serve as structural supports. The system is designed with an unprecedentedly low material budget, which is a requirement for particle detectors aiming to achieve precise tracking at low particle momenta. This innovative approach leads to an 80% reduction in material budget compared to the previous version (ITS2), resulting in enhanced measurement accuracy.

An experimental setup has been built to validate the proposed design. Heat dissipation of the layers has been modeled by including heaters of reduced thickness, and multiple temperature sensors have been installed to obtain the temperature distribution in the layers. The quality of the prototype in terms of dimensional tolerances has been verified with a computed tomography scan. The results of the scan have

also been used to validate the quality of the gluing process between the foams and the layers. A numerical model has been implemented, which treats the foams as porous mediums with averaged properties. The geometry and parameters of the experimental setup have been used in numerical simulations; in particular, to determine the thermal performance of the system in a case of practical application. The mean deviation between the experiments and the simulations in the temperature distributions is lower than 0.5 K. The simulations overpredict the temperature values, and this has been ascribed to the thermal resistance induced by the glue between the temperature sensors and the layers.

The experimental setup, though close to the ITS3 setup, does not exactly represent the configuration of the final detector. Simulations have been performed with the real geometry. With the reference values of heat dissipation obtained from other working groups, it has been proven that the design requirement in terms of temperature distribution is met with freestream velocity values of more than 5 $\mathrm{m\,s^{-1}}$. Since the layer heat dissipation values used in this work are approximate, a parametric study has been performed. An improvement in the baseline design has been proposed that provides almost a 50% reduction in the maximum temperature difference with respect to the baseline configuration.

The experimental and numerical results presented complete the thermal analysis of the system, in which no maximum value of the air freestream velocity has been specified. However, the air flow generates vibrations in the silicon layers, which may not be negligible given the high accuracy of the sensors. A numerical and experimental study of the vibrations is required to complete the design validation, which is expected to be part of future work.

Declaration of competing interest

The authors declare that they have no known competing financial interests or personal relationships that could have appeared to influence the work reported in this paper.

Data availability

No data was used for the research described in the article.

Acknowledgments

The authors acknowledge the "CERN EP-DT-DD Micro-Pattern Technologies (MPT) service" for the production of the integrated polyimide heaters, as well as the "CERN EN-MME Materials, Metrology and Non-Destructive Testing (MM) Section" for the realization of the computed tomography scan of the prototype. The authors also acknowledge Universidad Politécnica de Madrid for providing computing resources on the Magerit Supercomputer.

Appendix. Nomenclature

Table A.6
Subindexes and superindexes.

Symbol	Subindex
bp	Beam pipe
e	Endcap
f	Foam
m	Matrix
ref	Reference
s	Solid
t	Turbulent
∞	Freestream
p	Periphery
Symbol	**Superindex**
eq	Equivalent

Table A.7
Variables.

Symbol	Variable	Units
h	Specific enthalpy	$\mathrm{J\,kg^{-1}}$
k	Turbulent kinetic energy	$\mathrm{m^2}$
p	Pressure	Pa
T	Temperature	K
t	Time	s
v	Velocity	$\mathrm{m\,s^{-1}}$
x, y, z	Cartesian coordinates	m
φ	Azimuthal angle	rad
τ	Viscous stress tensor	Pa
ω	Turbulent specific dissipation rate	$\mathrm{s^{-1}}$

Table A.8
Parameters.

Symbol	Variable	Units
C_d	Drag coefficient	–
c_p	Specific heat at constant pressure	$\mathrm{J\,kg^{-1}\,K^{-1}}$
E	Young modulus	Pa
h	Heat transfer coefficient	$\mathrm{W\,m^{-2}\,K^{-1}}$
Pr	Prandtl number	–
$\mathcal{P}$	Permeability coefficient	$\mathrm{m^2}$
q	Heat flux	$\mathrm{W\,m^{-2}}$
Re	Reynolds number	–
κ	Thermal conductivity	$\mathrm{W\,m^{-1}\,K^{-1}}$
μ	Dynamic viscosity	Pa s
Φ	Porosity	–
ρ	Density	$\mathrm{kg\,m^{-3}}$
Σ	Specific surface area	$\mathrm{m^{-1}}$

References

[1] M. Chávez-Modena, L.M. González, E. Valero, A. Broatch, J. García-Tíscar, A. Felgueroso, Experimental and numerical methodology for the aero-thermal analysis of a SACOC heat exchanger, Appl. Therm. Eng. 219 (2023) 119409, http://dx.doi.org/10.1016/j.applthermaleng.2022.119409.

[2] J.C. Han, Recent studies in turbine blade cooling, Int. J. Rotating Mach. 10 (517231) (2014) http://dx.doi.org/10.1155/S1023621X04000442.

[3] I. Mudawar, D. Bharathan, K. Kelly, S. Narumanchi, Two-phase spray cooling of hybrid vehicle electronics, IEEE Trans. Compon. Packag. Technol. 32 (2) (2009) 501–512, http://dx.doi.org/10.1109/ITHERM.2008.4544399.

[4] S. Nagaya, N. Hirano, M. Naruse, T. Watanabe, T. Tamada, Development of a high-efficiency conduction cooling technology for SMES coils, IEEE Trans. Appl. Supercond. 23 (3) (2012).

[5] R.L. Webb, K. Chung, Two-phase flow distribution to tubes of parallel flow air-cooled heat exchangers, Heat Transfer Eng. 26 (4) (2005) 3–18, http://dx.doi.org/10.1080/01457630590916239.

[6] G. Wypych, Handbook of Foaming and Blowing Agents, second ed., ChemTec Publishing, 2022.

[7] Y. Wang, Y. Yu, Z. Jing, C. Wang, G. Zhou, W. Zhao, Thermal performance of lithium-ion batteries applying forced air cooling with an improved aluminium foam heat sink design, Int. J. Heat Mass Transfer 167 (120827) (2021) http://dx.doi.org/10.1016/j.ijheatmasstransfer.2020.120827.

[8] A. Amatriain, C. Gargiulo, G. Rubio, Numerical and experimental study of open-cell foams for the characterization of heat exchangers, Int. J. Heat Mass Transfer 217 (124701) (2023) http://dx.doi.org/10.1016/j.ijheatmasstransfer.2023.124701.

[9] ATLAS Collaboration, Technical Design Report for the ATLAS Inner Tracker Pixel Detector, Technical Report CERN-LHCC-2017-021, CERN, 2017.

[10] ATLAS Collaboration, Technical Design Report for the ATLAS Inner Tracker Strip Detector, Technical Report CERN-LHCC-2017-005, CERN, 2017.

[11] CMS Collaboration, The Phase-2 Upgrade of the CMS Tracker, Technical Report CERN-LHCC-2017-009, CERN, 2017.

[12] The ALICE Collaboration, Letter of Intent for an ALICE ITS Upgrade in LS3, Technical Report CERN-LHCC-2019-018, CERN, 2019.

[13] H. Kolanoski, N. Wermes, Particle Detectors: Fundamentals and Applications, Oxford University Press, 2020.

[14] ALICE Collaboration, Technical Design Report for the Upgrade of the ALICE Inner Tracking System, Technical Report CERN-LHCC-2013-024, CERN, 2013.

[15] S.G. Kandlikar, History, advances, and challenges in liquid flow and flow boiling heat transfer in microchannels: A critical review, J. Heat Transfer 134 (3) (2012) http://dx.doi.org/10.1115/1.4005126.
[16] S.J. Pety, M.H.Y. Tan, A.R. Najafi, P.R. Barnett, P.H. Geubelle, S.R. White, Carbon fiber composites with 2D microvascular networks for battery cooling, Int. J. Heat Mass Transfer 115 (2017) 513–522, http://dx.doi.org/10.1016/j.ijheatmasstransfer.2017.07.047.
[17] G. Contin, L. Greiner, J. Schambach, M. Szelezniak, E. Anderssen, J. Bell, et al., The STAR MAPS-based PiXeL detector, Nucl. Instrum. Methods Phys. Res., Sect. A 907 (2018) 60–80, http://dx.doi.org/10.1016/j.nima.2018.03.003.
[18] K. Arndt, H. Augustin, P. Baesso, N. Berger, F. Berg, C. Betancourt, et al., Technical design of the phase I Mu3e experiment, Nucl. Instrum. Methods Phys. Res., Sect. A 1014 (165679) (2021) http://dx.doi.org/10.1016/j.nima.2021.165679.
[19] T.T. Rudzki, F.M. Aeschbacher, M. Deflorin, N. Flucher, Successful cooling of a pixel tracker using gaseous helium: Studies with a mock-up and a detector prototype, Nucl. Instrum. Methods Phys. Res., Sect. A 168405 (2023) http://dx.doi.org/10.1016/j.nima.2023.168405.
[20] A. Kluge, ALICE - ITS3 — A bent, wafer-scale CMOS detector, Nucl. Instrum. Methods Phys. Res., Sect. A 1041 (2022) 167315, http://dx.doi.org/10.1016/j.nima.2022.167315.
[21] S. De Schampheleire, P. De Jaeger, H. Huisseune, B. Ameel, C. T'Joen, K. De Kerpel, M. De Paepe, Thermal hydraulic performance of 10 PPI aluminium foam as alternative for louvered fins in an HVAC heat exchanger, Appl. Therm. Eng. 51 (1) (2013) 371–382, http://dx.doi.org/10.1016/j.applthermaleng.2012.09.027.
[22] T. Rehman, H.M. Ali, Experimental study on the thermal behavior of RT-35HC paraffin within copper and iron-nickel open cell foams: Energy storage for thermal management of electronics, Int. J. Heat Mass Transfer 146 (118852) (2020) http://dx.doi.org/10.1016/j.ijheatmasstransfer.2019.118852.
[23] H. Ami Ahmadi, N. Variji, A. Kaabinejadian, M. Moghimi, M. Siavashi, Optimal design and sensitivity analysis of energy storage for concentrated solar power plants using phase change material by gradient metal foams, J. Energy Storage 35 (102233) (2021) http://dx.doi.org/10.1016/j.est.2021.102233.
[24] B.J. McKeon, M.V. Zagarola, A.J. Smits, A new friction factor relationship for fully developed pipe flow, J. Fluid Mech. 538 (2005) 429–443, http://dx.doi.org/10.1017/S0022112005005501.
[25] S.B. Pope, Turbulent Flows, Cambridge University Press, 2000.
[26] F.R. Menter, Two-equation Eddy-viscosity turbulence models for engineering applications, AIAA J. 32 (8) (1994) 1598–1605, http://dx.doi.org/10.2514/3.12149.
[27] J. Bear, Modeling Phenomena of Flow and Transport in Porous Media, Springer, 2018.
[28] W.M. Kays, Turbulent Prandtl number—Where are we? J. Heat Transfer 116 (2) (1994) 284–295, http://dx.doi.org/10.1115/1.2911398.
[29] C.E. Brennen, Fundamentals of Multiphase Flows, Cambridge University Press, 2005.
[30] D.C. Wilcox, Turbulence Modeling for CFD, third ed., DCW Industries, 2006.
[31] Ansys Inc., Ansys Fluent Theory Guide, 2023R1, 2023.
[32] S. Majumdar, Role of underrelaxation in momentum interpolation for calculation of flow with nonstaggered grids, Numer. Heat Transfer 13 (1) (1988) 125–132, http://dx.doi.org/10.1080/10407788808913607.
[33] M. Darwish, I. Sraj, F. Moukalled, A coupled finite volume solver for the solution of incompressible flows on unstructured grids, J. Comput. Phys. 228 (1) (2009) 180–201, http://dx.doi.org/10.1016/j.jcp.2008.08.027.
[34] S.F. McCormick, Multigrid Methods, SIAM, 1987, http://dx.doi.org/10.1137/1.9781611971057.
[35] R.B. Boss, Metallic Materials Specification Handbook, fourth ed., Springer, 1991.
[36] A. Masolin, P.O. Bouchard, R. Martini, M. Bernacki, Thermo-mechanical and fracture properties in single-crystal silicon, J. Mater. Sci. 48 (2013) 979–988, http://dx.doi.org/10.1007/s10853-012-6713-7.
[37] H. Schlichting, Boundary Layer Theory, seventh edition, McGraw-Hill, 1979.